

Numerical Modelling of Galvanic Corrosion of WE43 Mg Alloy in Blood Bank Buffered Saline Solution

Hesham Mraied and Asma Sharfeddin

Department of Materials and Metallurgical Engineering, University of Tripoli
E-mail: h.mraied@uot.edu.ly

Abstract

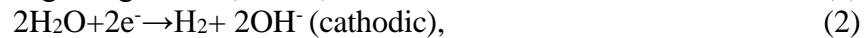
The effect of the microstructure on the corrosion behavior of WE 43 Mg alloy in blood bank buffered saline solution was simulated using COMSOL Multiphysics finite element platform. The model was also implemented to estimate the electrode kinetic parameters based on potentiodynamic polarization experiments. The model was able to track the moving boundary of the corroding anode of the micro-galvanic couple. The corrosion rates estimated from the model were in good agreement with the corresponding experimental values. The model predicted that the dissolution rate of the anode increases by increasing the size fraction of the precipitates (cathode). The thickness of metal loss was 2.7 μm , 5.7 μm and 9.6 μm for the 20 %, 40 % and 60 % precipitate size fraction, respectively.

Keywords: WE43 Mg alloy, corrosion, COMSOL Multiphysics, polarization, Modelling.

1. Introduction

Biodegradable WE43 Mg alloy has been recently considered for biological applications such as temporary cardiovascular stents [1, 2] and bone implants [3, 4]. In contrast to conventional bio metallic materials such as titanium, cobalt-chromium, and stainless steels, Mg can safely degrade in the human body; hence no post operation is required once the damaged tissue is healed. This will minimize procedure cost and risks [5, 6]. Moreover, Mg alloys exhibit good cell adhesion in physiological environment and considered as an essential element for human metabolic processes [7-9].

Unfortunately, Mg alloys exhibit high degradation rate in physiological environments [10, 11] leading to unfavorable structural integrity loss and extensive hydrogen evolution [12, 13] as shown in equations 1 and 2. The electrons released by the anodic reaction are consumed by the cathodic reaction to generate H_2 gas [14]. The Mg^{2+} and OH^- ions formed by the anodic and cathodic reactions, respectively, will then combine to form a $\text{Mg}(\text{OH})_2$ film according to equation 3 [15, 16];



Alloying of Mg with proper alloying elements is a common practice to enhance its mechanical properties, but this is usually associated with reduced corrosion resistance. In general, the corrosion resistance of pure Mg is generally higher than that of its alloys [17]. The formation

of (less electrochemically active) precipitates and secondary phases often leads to undesired micro-galvanic coupling between the precipitates and the (more electrochemically active) α -Mg matrix. In general, these precipitates will serve as micro-cathodes while the α -Mg matrix will serve as the micro-anode and preferentially dissolve in the electrolyte solution [18].

It was reported that a proper microstructure modification including minimizing precipitation and formation of a chemically homogeneous supersaturated solid led to a reduction of corrosion rate of WE43 alloy by more than one order of magnitude compared to the conventionally cast alloy [19]. Minimizing precipitates size can significantly reduce cathode size hence, slowed down the cathodic reaction kinetics. Hanzi et al. [20] created different surface conditions of WE43 Mg alloy by different heat treatment regimes and reported the enhancement of corrosion resistance after heat treatment. Subasi et al. [21] investigated the effects of intermetallic compound and Long-period stacking ordered (LPSO) Zn rich phases on the corrosion resistance of as-cast and as-extruded WE43-xZn. They concluded that the corrosion resistance of the as-cast alloy was improved due to the presence of LPSO structure, while the presence and distribution of the intermetallic compounds varied the corrosion resistance of the as-extruded alloy.

While the researches described above are experimental in nature, in which the corrosion resistance of WE43 Mg alloy was found to improve by minimizing fractions of precipitations and secondary phases. In this work, a predictive corrosion modelling was implemented to provide quantitative estimation of the effect of precipitates size on the corrosion behavior of WE 43 Mg alloy. The corrosion kinetic parameters of the polarization behavior of the alloy were obtained from potentiodynamic polarization experiments of WE 43 Mg alloy in blood bank buffered saline solution [19]. The model was built on a Comsol Multiphysics finite element platform (COMSOL). The model explored possible ways in which tailoring the microstructure of WE43 Mg alloy can alter the corrosion behavior. The model assumed that active corrosion was taking place on only a part of the alloy surface (anode), and examined the possible effect of enhanced micro-galvanic corrosion when the passive portion of the surface (cathode) became larger.

2. Computational

2.1 Estimation of kinetic parameters

To overcome the challenges to accurately determine the electrode kinetics as a function of electrode potential, the optimization interface of COMSOL was used to perform electrode kinetics parameters estimation based on the polarization data. A zero-dimensional electrode polarization model was built using anode and cathode Tafel expression for the metal dissolution (equation 1) and oxygen reduction (equation 2) reactions. Kinetic parameters were estimated using a global least squares objective function based on the electrochemical polarization test of WE43 Mg alloy in blood bank buffered saline solution. This objective function represents the sum of squared differences between measurements stored in an experiment data file and a corresponding expression evaluated by COMSOL.

The dissolution reaction of the alloy was described by anodic Tafel equation as;

$$i_a = i_{oa} \times 10^{((E-E_{oa})/\beta_a)} \quad (4)$$

where i_{oa} (A/m^2) is the exchange current density and β_a (V) is the anodic Tafel slope of the metal dissolution reaction, respectively. E is the potential of the alloy minus that of the electrolyte as measured by a reference electrode ideally placed in the electrolyte at a point immediately next to

the metal surface. E_{oa} is the equilibrium potential of the metal dissolution reaction. In this model $E_{oa} = 0$ as the cathodic part of the metal dissolution reaction is neglected.

The cathodic oxygen reduction reaction was described by the following Tafel expression;

$$i_c = -i_{oc} \times 10^{((E_{oc}-E)/\beta_c)} \quad (5)$$

where i_{oc} (A/m^2) is the exchange current density and β_c (V) is the cathodic Tafel slope of the oxygen reduction reaction, respectively.

Finally, the net current density at the electrode surface, i (A/m^2), is:

$$i = i_c + i_a \quad (6)$$

It should be noted here that hydrogen evolution reaction was not considered in this model as another possible cathodic reaction. The model is formulated as a set of parametric expressions in 0D and a Global-Least Squares node is used to construct the objective function used for optimization. The anodic and cathodic kinetic parameters in table 1 were assigned values that approximated the results of electrochemical polarization test of WE43 Mg alloy in blood bank buffered saline solution.

The input parameters in table 1 were used to numerically solve equations (4) through (6) simultaneously to calculate the kinetic parameters (i_{oa} , β_a , i_{oc} , and β_c).

Table 1. Parameter and Variable Descriptions and Values

Parameter /variable	Description	Value
E_{oa}	Equilibrium potential for metal dissolution	-1.7[V]
i_{oa}	Exchange current density for metal dissolution	0.001[A/m ²]
β_a	Anodic Tafel slope for metal dissolution	50[mV]
E_{oc}	Equilibrium potential of oxygen reduction	-1.2[V]
i_{oc}	Exchange current density for oxygen reduction	0.01[A/m ²]
β_c	Cathodic Tafel slope for oxygen reduction	-300[mV]
E	Electrode potential	-1.55[V]
i_a	Current density for metal dissolution	$i_a = i_{oa} \times 10^{((E-E_{oa})/\beta_a)}$
i_c	Current density for oxygen reduction	$i_c = -i_{oc} \times 10^{((E_{oc}-E)/\beta_c)}$
i	Local current density	$i_a + i_c$

2.2 Micro-galvanic corrosion simulation

The system simulated is shown in figure 1. The surface of the alloy exposed to the electrolyte is 100 μm long. A centrally located (x) μm long segment of the alloy (thus $x\%$ of its surface, representing the size fraction of the precipitates) was designed as a passive region where cathodic reactions take place. The rest of the surface area was considered as an actively corroding region where anodic reaction takes place. In this study, three values of (x) value were considered (20%, 40% and 60%) to simulate the effect of changing the size of precipitates (cathode) on the corrosion resistance of WE43 Mg alloy. The electrolyte was treated for simplicity as a homogeneous medium with uniform electrical and mass transport parameters.

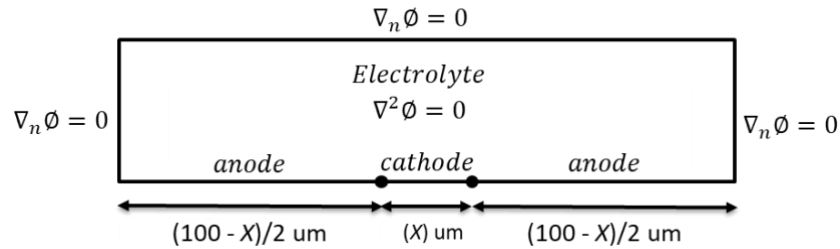


Fig. 1 Schematic diagram of WE43 Mg alloy microstructure configuration

The predominant anodic and cathodic reactions on the WE43 Mg alloy surface were assumed to be respectively Mg dissolution (equation 1) and oxygen reduction (equation 2, consistent with the usual alkaline conditions in physiological environment).

For the main series of calculations, the alloy-electrolyte system was regarded as having an electrically insulating external surface, and oxygen flow through the boundaries was not allowed ($\nabla_n \phi = 0$). The polarization behavior for active dissolution and oxygen reduction was determined following Butler-Volmer kinetics [22]. The anodic reaction taking place on the anodic region is given by equation 4, while the cathodic reaction was chosen to take place on the passive region on the alloy according to equation 5.

The mass flux (N) of oxygen associated with its reduction at passive region (cathode) of the WE43 Mg alloy is given by;

$$N = ic/(n * F) \quad (7)$$

Where n is the valence of the metal and F is Faraday's constant (96,500 C/mole)

In a time dependent coordinate system, the current density distribution in the electrolyte domain is given by a general form of ohm's law;

$$J = \sigma E_f \quad (8)$$

where J is the current density (A/m²), σ is the electrical conductivity of the electrolyte (S/m) and E_f is the electric field (V/m).

In this model a diffusional transport mechanism of oxygen was selected, where the mass balance is given in the bulk of the electrolyte by;

$$\frac{\partial c_o}{\partial t} + \nabla \cdot (-D_o \nabla c_o) = 0 \quad (9)$$

where c_o is the concentration (mol/m³) and D_o is the diffusion coefficient (m²/s) of oxygen, respectively.

Using the Arbitrary Lagrangian-Eulerian (ALE) application mode in COMSOL allows the tracking of moving interfaces. In this study, the anode boundary will move due to the dissolution of the alloy with velocity v (m/s) in the normal direction, according to

$$v = \frac{i_a M}{2F \rho} \quad (10)$$

where M is the molecular weight and ρ is the density of the WE43 Mg alloy. The values of which are listed in table 2.

Table 2 lists model parameters and their respective values, plus additional parameter values used in the model. The cathodic and anodic parameters (i_{oc} , i_{oa} , β_c , and β_a) were assigned values obtained from electrode kinetics parameters estimation (section 2.1) based on polarization data of WE43 Mg alloy in blood bank buffered saline solution. All potentials are given in the silver / silver chloride (Ag/AgCl) scale.

Equations (4) through (9) were solved simultaneously by the Time Dependent Study feature of COMSOL to yield the electrical potential and oxygen concentration in the electrolyte, from which the corresponding current densities at the alloy surface are derived. Simulations were performed using the finest predefined element size setting in the model platform, labeled as “Extra Fine”.

Table 2. Parameter and Variable Descriptions and Values

Parameter /variable	Description	Value
E_{oa}	Equilibrium potential for metal dissolution	-1.7[V]
i_{oa}	Exchange current density for metal dissolution	0.001
β_a	Anodic Tafel slope for metal dissolution	55[mV]
E_{oc}	Equilibrium potential of oxygen reduction	-1.2[V]
i_{oc}	Exchange current density for oxygen reduction	0.1[A/m ²]
β_c	Cathodic Tafel slope for oxygen reduction	-350[mV]
sigma	Electrolyte conductivity	5[S/m]
rho_Mg	Magnesium density	1820[kg/m ³]
M_Mg	Magnesium molecular weight	0.025[kg/mol]
L	Exposed length of the alloy	100 [um]

3. Results and Discussion

Figure 2 shows the experimental and model fit polarization curves of WE43 Mg alloy in blood bank buffered saline solution. It is clear that with the proposed model, a good fit was achieved for the experimental data. The kinetic parameters obtained from the model were as follows; $i_{oa} = 0.001$ A/m², $\beta_a = 55$ mV, $i_{oc} = 0.1$ A/m², and $\beta_c = -350$ mV. These output parameters were used as input parameters (table 2) for modeling the effect of precipitates size fraction on the corrosion behavior of WE43 Mg alloy.

The change in the electric potential over the electrolyte domain and the change in alloy thickness (dissolution of anodic domain) at different cathode sizes ($x = 20\%$, 40% and 60%) are shown in figure 3. It can be seen that the electric potential varies from -1.50 V vs. (Ag/AgCl) over the cathodic region to -1.58 V vs. (Ag/AgCl) over the anodic region up to 24 hours of exposure. It should be noted that the potential of the galvanic couple is estimated to be -1.53 V vs. (Ag/AgCl) from the experimental potentiodynamic tests as seen in figure 2. The potential gradient is also

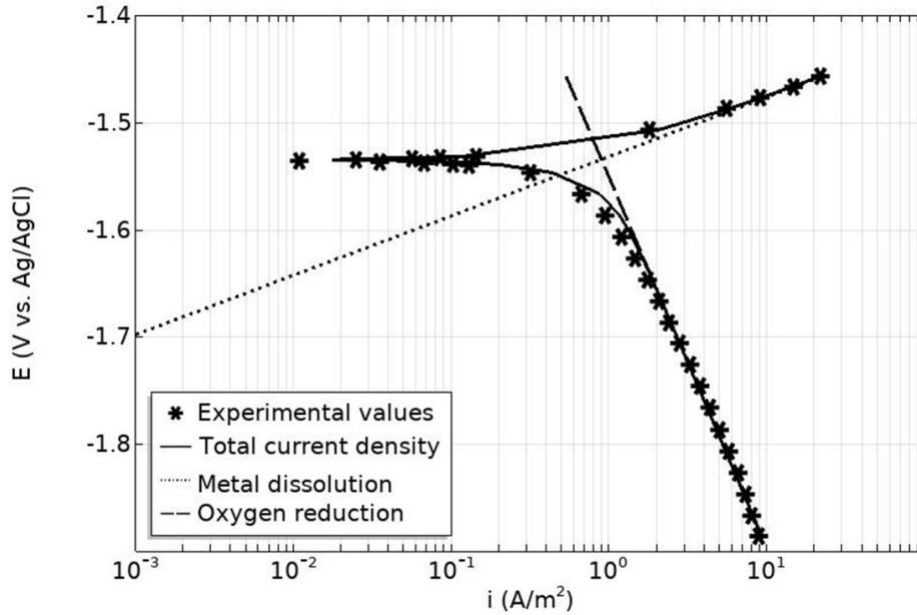


Fig. 2. Experimental (symbol) polarization curves and model fit (line) of WE43 Mg alloy in blood bank buffered saline solution.

shown in figure 3 in the form of arrows overlaid on the surface plot of the electric potential, which indicates the electric field induced from the lower potential region (anode) to the higher potential region (cathode). This electric field drives the dissolution of Mg into the electrolyte solution.

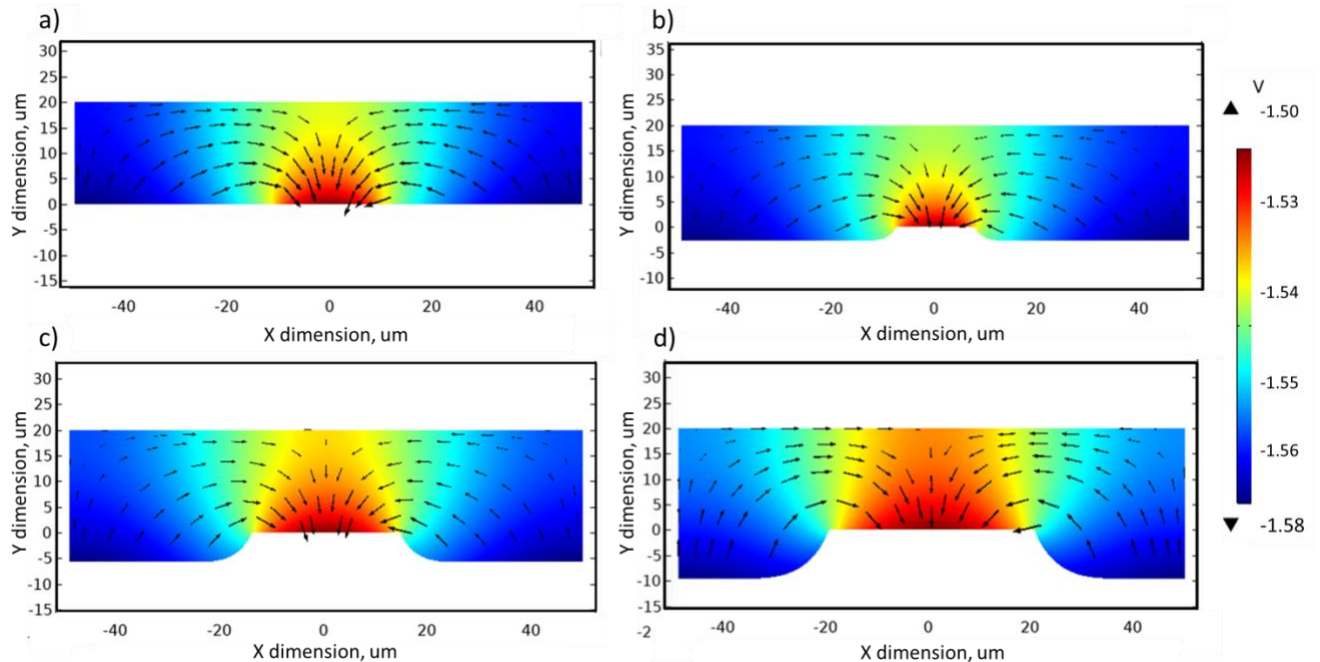


Fig. 3 Surface plot of electric potential and a contour plot of absolute potential gradient of WE43 Mg

alloy at different precipitate fractions for (a) $x=20\%$, $t=0$ hr, (b) $x=20\%$, $t=24$ hr, (c) $x=40\%$, $t=24$ hr, (d) $x=60\%$, $t=24$ hr.

As shown in figure 3, the output of model simulation agreed with expected scenarios of anode preferential dissolution in the electrolyte. The contour plot of the absolute potential gradient indicates the current density is the highest at the interface between the anode and the cathode. This would lead to a higher dissolution of the alloy at that interface and the dissolution rate decreases along the distance away from the anode. The model predicted that by increasing the size of the cathode, the thickness of metal loss increases as indicated by the change in Y-dimension axis in figure 3.

The change in current density along the anode and the cathode surfaces is plotted in figure 4. It can be seen that in general the current density at the anodic region are more negative compared to those at the cathode region. The current density profile over the anodic and the cathodic regions calculated from the numerical model agrees well with the potentiodynamic polarization experiment shown in figure 2. As expected, the current density was found to increase by increasing the size fraction of the precipitate. Since the dissolution reaction occurs at the anodic region of the micro-galvanic couple, the anodic current density will be considered for the corrosion rate estimate (surface thickness loss) of the alloy.

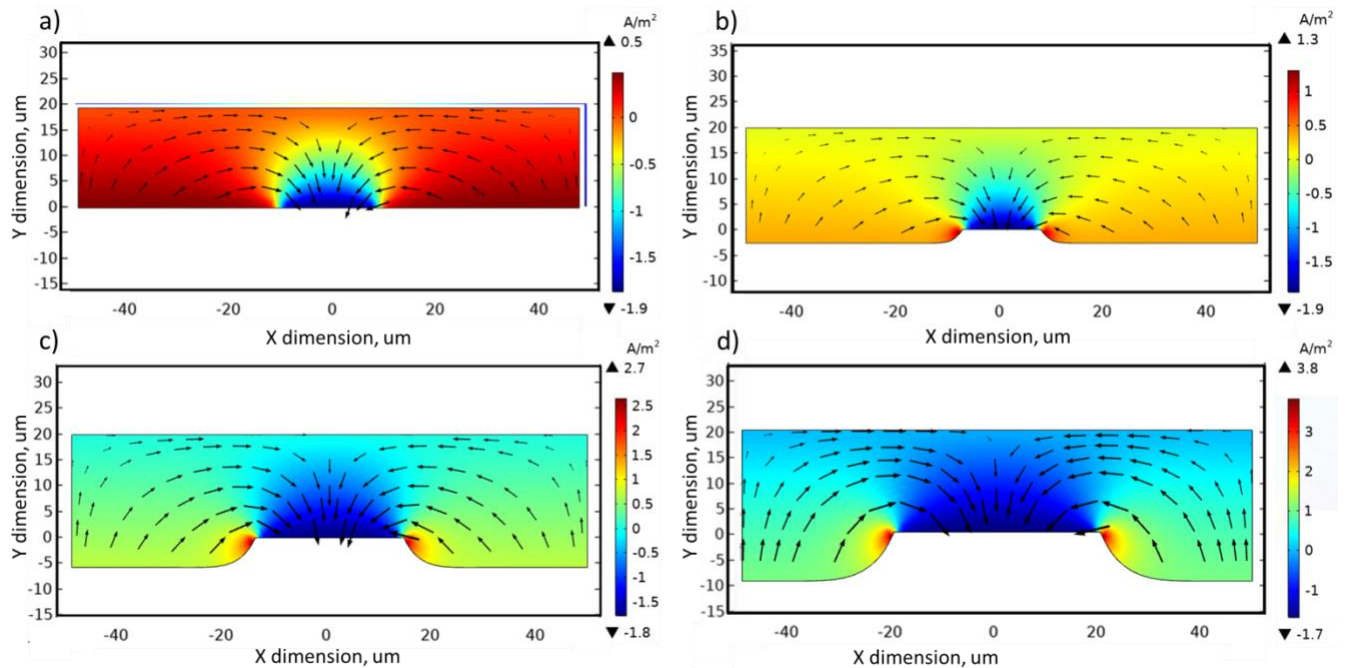


Fig. 4 Surface plot of electric current and a contour plot of absolute electric current density of WE43 Mg alloy at different precipitate fractions for (a) $x=20\%$, $t=0$ hr, (b) $x=20\%$, $t=24$ hr, (c) $x=40\%$, $t=24$ hr, (d) $x=60\%$, $t=24$ hr.

Figure 5 shows the time-integrated corrosion rate expressed as local thickness loss in μm after 24 hour exposure to the electrolyte. The model calculated the thickness loss by Faradaic conversion after integrating the anodic current densities in A/m^2 . The thickness of metal loss was $2.7 \mu\text{m}$ for $x=20\%$, $5.7 \mu\text{m}$ for $x=40\%$ and $9.6 \mu\text{m}$ for $x=60\%$. In other words, the amount of metal dissolution taking place at the anode surface (equation 1) increases to compensate for the oxygen reduction cathodic reaction taking place at the cathode (equation 2). The results were in good

agreement with the experimental values reported in the literature for the corrosion of Mg and its alloys in similar environments [23], and are plotted in figure 5 as a function of the position in the alloy segment length.

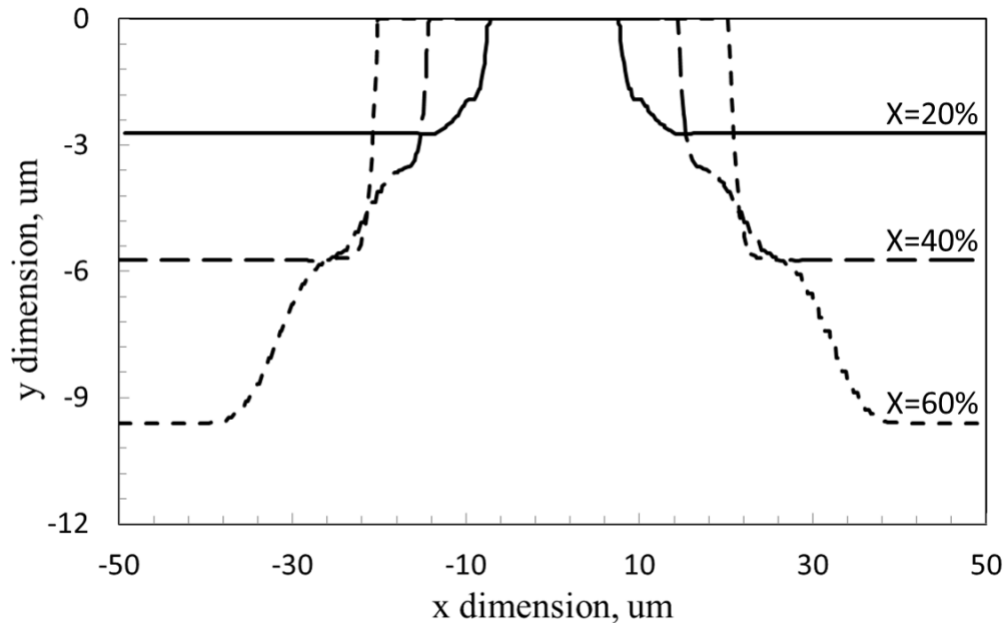


Fig. 5 effect of precipitation size change on the metal thickness of WE43 Mg alloy after 24 hours of immersion in blood bank buffered solution

4. Conclusions

1. A numerical model was implemented to track the moving boundary during micro-galvanic corrosion of WE43 Mg alloy.
2. The electrode kinetic parameters were estimated from potentiodynamic polarization experiments using numerical simulation.
3. The corrosion rate of the alloy was estimated after 24 hours of exposure to blood bank buffered saline solution.
4. The corrosion rates obtained from numerical modeling were in good agreement to those values obtained experimentally.
5. Modeling projections indicated that the corrosion rate of the alloy increased by increasing the size fraction of the precipitates (size of the cathode).
6. The thickness of metal loss was 2.7 um, 5.7 um and 9.6 um for 20 %, 40 % and 60 % precipitate size fraction, respectively.

References

1. Waksman, R., et al., *Safety and efficacy of bioabsorbable magnesium alloy stents in porcine coronary arteries*. Catheterization and Cardiovascular Interventions, 2006. **68**(4): p. 607-617.
2. Heublein, B., et al., *Biocorrosion of magnesium alloys: a new principle in cardiovascular implant technology?* Heart, 2003. **89**(6): p. 651-656.
3. Jin, W., et al., *Improvement of corrosion resistance and biocompatibility of rare-earth WE43 magnesium alloy by neodymium self-ion implantation*. Corrosion Science, 2015. **94**: p. 142-155.
4. Witte, F., et al., *In vitro and in vivo corrosion measurements of magnesium alloys*. Biomaterials, 2006. **27**(7): p. 1013-1018.
5. Castellani, C., et al., *Bone-implant interface strength and osseointegration: Biodegradable magnesium alloy versus standard titanium control*. Acta Biomaterialia, 2011. **7**(1): p. 432-440.
6. Weiler, A., et al., *Biodegradable Implants in Sports Medicine: The Biological Base*. Arthroscopy: The Journal of Arthroscopic & Related Surgery, 2000. **16**(3): p. 305-321.
7. Liu, N., et al., *Electrochemical corrosion behavior of Mg-5Al-0.4Mn-xNd in NaCl solution*. Corrosion Science, 2009. **51**(6): p. 1328-1333.
8. Zhao, Y., et al., *Enhanced antimicrobial properties, cytocompatibility, and corrosion resistance of plasma-modified biodegradable magnesium alloys*. Acta Biomaterialia, 2014. **10**(1): p. 544-556.
9. Feyerabend, F., et al., *Evaluation of short-term effects of rare earth and other elements used in magnesium alloys on primary cells and cell lines*. Acta Biomaterialia, 2010. **6**(5): p. 1834-1842.
10. Song, G., *Control of biodegradation of biocompatible magnesium alloys*. Corrosion Science, 2007. **49**(4): p. 1696-1701.
11. Xin, Y., T. Hu, and P.K. Chu, *In vitro studies of biomedical magnesium alloys in a simulated physiological environment: A review*. Acta Biomaterialia, 2011. **7**(4): p. 1452-1459.
12. Atrens, A., M. Liu, and N.I. Zainal Abidin, *Corrosion mechanism applicable to biodegradable magnesium implants*. Materials Science and Engineering B: Solid-State Materials for Advanced Technology, 2011. **176**(20): p. 1609-1636.
13. Kirkland, N.T., G. Williams, and N. Birbilis, *Observations of the galvanostatic dissolution of pure magnesium*. Corrosion Science, 2012. **65**: p. 5-9.
14. Frankel, G.S., A. Samaniego, and N. Birbilis, *Evolution of hydrogen at dissolving magnesium surfaces*. Corrosion Science, 2013. **70**: p. 104-111.
15. Thomas, S., et al., *Corrosion mechanism and hydrogen evolution on Mg*. Current Opinion in Solid State and Materials Science, 2015. **19**(2): p. 85-94.
16. Gusieva, K., et al., *Corrosion of magnesium alloys: the role of alloying*. International Materials Reviews, 2015. **60**(3): p. 169-194.
17. Song, G.L. and A. Atrens, *Corrosion mechanisms of magnesium alloys*. Advanced Engineering Materials, 1999. **1**(1): p. 11-33.
18. Song, Y.W., D.Y. Shan, and E.H. Han, *Pitting corrosion of a Rare Earth Mg alloy GW93*. Journal of Materials Science & Technology, 2017. **33**(9): p. 954-960.

19. Mraied, H., W. Wang, and W. Cai, *Influence of chemical heterogeneity and microstructure on the corrosion resistance of biodegradable WE43 magnesium alloys*. Journal of Materials Chemistry B, 2019 ,**7**, 6399-6411.
20. Hänzi, A.C., et al., *On the biodegradation performance of an Mg–Y–RE alloy with various surface conditions in simulated body fluid*. Acta Biomaterialia, 2009. **5**(1): p. 162-171.
21. Subasi, Y., et al., *Effect of Zn addition on mechanical and corrosion properties of as-cast and as-extruded WE43 magnesium alloys*. Materials Research Express, 2019. **6**(11): p. 1165f9.
22. Kranc, S.C. and A.A. Sagüés, *Computation of Reinforcing Steel Corrosion Distribution in Concrete Marine Bridge Substructures*. CORROSION, 1994. **50**(1): p. 50-61.
23. Atrens, A., et al., *Review of Mg alloy corrosion rates*. Journal of Magnesium and Alloys, 2020. **8**(4): p. 989-998.